AN IMPLICIT SCHEME FOR INCOMPRESSIBLE FLOW COMPUTATION WITH ARTIFICIAL COMPRESSIBILITY METHOD

Nguyen The Duc

Institute of Mechanics, Vietnamese Academy of Science and Technology

Abstract. To simulate the incompressible flow in complex three-dimensional geometry efficiently and accurately, a solver based on solution of the Navier-Stokes equations in the generalized curvilinear coordinate system was developed. The system of equations in three-dimension are solved simultaneously by the artificial compressibility method. The convective terms are differenced using a flux difference splitting approach. The viscous terms are differenced using second-order accurate central differences. An implicit line relaxation scheme is employed to solve the numerical system of equations. The solver was tested for two cases including flow past a circular cylinder and flow around a hemispherical head of a cylindrical object.

1. Introduction

Solutions to the incompressible Navier-Stokes equations are of interest in many fields of computational fluid dynamics. The problem of coupling changes in the velocity field with changes in pressure field while satisfying the continuity equation is the main difficulty in obtaining solutions to the incompressible Navier-Stokes. There are some types of method have been developed to solve the equations. The stream-function vorticity formulation of the equation has been used often when only two-dimensional problems are of interest, but this has no straightforward extension.

Other methods using primitive variables can be classified into two groups. The first group of methods can be classified as pressure-based methods. In these methods, the pressure field is solved by combining the momentum and mass continuity equations for form a pressure or pressure-correction equation ([1], [2]).

The second group of methods employs the artificial compressibility formulation. This idea was first introduced by Chorin [3] for use in obtaining steady-state solutions to the incompressible flow. Several authors have employed this method successfully in computing unsteady problems. Mercle and Athavale [4] presented solution using this approach in two-dimensional generalized coordinates. Park and Sankar [5] also present solutions for three-dimensional problem using explicit scheme.

The paper presents an implicit solution procedure using the method of artificial compressibility. For numerical accuracy and stability, the convective terms are differenced by and an upwind scheme based on the method of Roe [6] that is biased by the sign of the eigenvalues of local flux Jacobian. The time-dependent solution is obtained by subiterating at each physical time step and driving the divergence of velocity toward zero.

In the following sections, the mathematical basis of the method is presented, including the governing equation and the transformation into generalized curvilinear coordinates. The specific details of the upwind scheme are given, follow by the details of the implicit line relaxation scheme used to solve the equations. The computed results show the robustness and accuracy of the code by presenting two sample problems, the flow past a circular cylinder and the flow around a hemispherical head of a cylindrical object.

2. Governing Equations in the Physical Domain

Three-dimensional incompressible Reynolds averaged Navier-Stokes equation in a Cartesian coordinate system may be written as follow:

$$\frac{\partial Q}{\partial t} + \frac{\partial (E - E_\nu)}{\partial x} + \frac{\partial (F - F_\nu)}{\partial y} + \frac{\partial (G - G_\nu)}{\partial z} = 0 \tag{1}$$

where Q, E, F, G, E_ν, F_ν and G_ν are vectors defined as:

$$Q = \begin{bmatrix} 0 \\ u \\ v \\ w \end{bmatrix} \;;\; E = \begin{bmatrix} u \\ u^2 + p/\rho \\ uv \\ uw \end{bmatrix} \;;\; F = \begin{bmatrix} v \\ uv \\ v^2 + p/\rho \\ vw \end{bmatrix} \;;\; G = \begin{bmatrix} w \\ uw \\ vw \\ w^2 + p/\rho \end{bmatrix}$$

$$E_\nu = \rho^{-1} \begin{bmatrix} 0 \\ \tau_{xx} \\ \tau_{xy} \\ \tau_{xz} \end{bmatrix} \;;\; F_\nu = \rho^{-1} \begin{bmatrix} 0 \\ \tau_{yx} \\ \tau_{yy} \\ \tau_{yz} \end{bmatrix} \;;\; G_\nu = \rho^{-1} \begin{bmatrix} 0 \\ \tau_{zx} \\ \tau_{zy} \\ \tau_{zz} \end{bmatrix} \tag{2}$$

The quantity, ρ, is the fluid density, p is the pressure, and u, v and w are the Cartesian components of velocity. The stress term given by

$$\begin{aligned}
\tau_{xx} &= \frac{2}{3}(\mu + \mu_t)(2\frac{\partial u}{\partial x} - \frac{\partial v}{\partial y} - \frac{\partial w}{\partial z}) \quad ; \quad \tau_{xy} = (\mu + \mu_t)(\frac{\partial u}{\partial y} + \frac{\partial v}{\partial x}) = \tau_{yx} \\
\tau_{yy} &= \frac{2}{3}(\mu + \mu_t)(2\frac{\partial v}{\partial y} - \frac{\partial u}{\partial x} - \frac{\partial w}{\partial z}) \quad ; \quad \tau_{xz} = (\mu + \mu_t)(\frac{\partial w}{\partial x} + \frac{\partial u}{\partial z}) = \tau_{zx} \\
\tau_{zz} &= \frac{2}{3}(\mu + \mu_t)(2\frac{\partial w}{\partial z} - \frac{\partial u}{\partial x} - \frac{\partial v}{\partial y}) \quad ; \quad \tau_{yz} = (\mu + \mu_t)(\frac{\partial v}{\partial z} + \frac{\partial w}{\partial y}) = \tau_{zy}
\end{aligned} \tag{3}$$

where μ is the laminar viscosity and μ_t is the turbulent viscosity.

The above set of equation is put into non-dimensional form by scaling as follows:

$$x^* = \frac{x}{L} \;;\; y^* = \frac{y}{L} \;;\; z^* = \frac{z}{L} \quad ; \quad u^* = \frac{u}{V} \;;\; v^* = \frac{v}{V} \;;\; w^* = \frac{w}{V}$$

$$p^* = \frac{p}{\rho V^2} \quad ; \quad t^* = \frac{t}{(L/V)} \quad ; \quad \mu_t^* = \frac{\mu_t}{\mu} \tag{4}$$

where the non-dimensional variables are denoted by an asterisk. V is the reference velocity and L is the reference length used in the Reynolds number

$$Re = \frac{\rho V L}{\mu}$$

By applying this non-dimensionalizing procedure (4) to Equations (1)-(3), the following non-dimensional equations are obtained:

$$\frac{\partial Q^*}{\partial t^*} + \frac{\partial (E^* - E_\nu^*)}{\partial x^*} + \frac{\partial (F^* - F_\nu^*)}{\partial y^*} + \frac{\partial (G^* - G_\nu^*)}{\partial z^*} = 0 \tag{5}$$

where

$$Q^* = \begin{bmatrix} 0 \\ u^* \\ v^* \\ w^* \end{bmatrix} \;;\; E^* = \begin{bmatrix} u^* \\ u^{*2} + p^* \\ u^* v^* \\ u^* w^* \end{bmatrix} \;;\; F^* = \begin{bmatrix} v^* \\ u^* v^* \\ v^{*2} + p^* \\ v^* w^* \end{bmatrix} \;;\; G^* = \begin{bmatrix} w^* \\ u^* w^* \\ v^* w^* \\ w^{*2} + p^* \end{bmatrix}$$

$$E_\nu^* = \frac{1}{Re} \begin{bmatrix} 0 \\ \tau_{xx}^* \\ \tau_{xy}^* \\ \tau_{xz}^* \end{bmatrix} \;;\; F_\nu^* = \frac{1}{Re} \begin{bmatrix} 0 \\ \tau_{yx}^* \\ \tau_{yy}^* \\ \tau_{yz}^* \end{bmatrix} \;;\; G_\nu^* = \frac{1}{Re} \begin{bmatrix} 0 \\ \tau_{zx}^* \\ \tau_{zy}^* \\ \tau_{zz}^* \end{bmatrix} \tag{6}$$

here

$$\tau_{xx}^* = \frac{2}{3}(1+\mu_t^*)(2\frac{\partial u^*}{\partial x^*} - \frac{\partial v^*}{\partial y^*} - \frac{\partial w^*}{\partial z^*}) \quad ; \quad \tau_{xy}^* = (1+\mu_t^*)(\frac{\partial u^*}{\partial y^*} + \frac{\partial v^*}{\partial x^*}) = \tau_{yx}^*$$

$$\tau_{yy}^* = \frac{2}{3}(1+\mu_t^*)(2\frac{\partial v^*}{\partial y^*} - \frac{\partial u^*}{\partial x^*} - \frac{\partial w^*}{\partial z^*}) \quad ; \quad \tau_{xz}^* = (1+\mu_t^*)(\frac{\partial w^*}{\partial x^*} + \frac{\partial u^*}{\partial z^*}) = \tau_{zx}^* \tag{7}$$

$$\tau_{zz}^* = \frac{2}{3}(1+\mu_t^*)(2\frac{\partial w^*}{\partial z^*} - \frac{\partial u^*}{\partial x^*} - \frac{\partial v^*}{\partial y^*}) \quad ; \quad \tau_{yz}^* = (1+\mu_t^*)(\frac{\partial v^*}{\partial z^*} + \frac{\partial w^*}{\partial y^*}) = \tau_{zy}^*$$

Note that the non-dimensional form of the governing equations given by Equations (5) is identical (except for the asterisks) to the dimensional form given by Equations (1). For convenience, from now on the asterisks will be dropped from the non-dimensional equations.

3. Governing Equations in the Computational Domain

If governing equations in a Cartesian system are directly used to flow past complex geometry, the imposition of boundary conditions will require a complicated interpolation of the data on local grid lines since the computational boundaries of complex geometry do not coincide with coordinate lines. This leads to a local loss of accuracy in the computed solutions. To avoid these difficulties, a transformation from the physical domain (Cartesian coordinates (x, y, z)) to computational domain (generalized curvilinear (ξ, η, ζ)) is used. This means a distorted domain in the physical space is transformed in to a uniformly spaced rectangular domain in the generalized coordinate space [7].

If we assume that there is a unique, single-valued relationship between the generalized coordinates and the physical coordinate and let the general transformation be given by

$$\xi = \xi(x, y, z) \quad ; \quad \eta = \eta(x, y, z) \quad ; \quad \zeta = \zeta(x, y, z)$$

then the governing equation (5) can be transformed as:

$$\frac{\partial \hat{Q}}{\partial t} + \frac{\partial (\hat{E} - \hat{E}_\nu)}{\partial \xi} + \frac{\partial (\hat{F} - \hat{F}_\nu)}{\partial \eta} + \frac{\partial (\hat{G} - \hat{G}_\nu)}{\partial \zeta} = 0 \tag{8}$$

where

$$\hat{Q} = \frac{1}{J}\begin{bmatrix} 0 \\ u \\ v \\ w \end{bmatrix} ; \hat{E} = \frac{1}{J}\begin{bmatrix} U \\ uU + p\xi_x \\ vU + p\xi_y \\ wU + p\xi_z \end{bmatrix} ; \hat{F} = \frac{1}{J}\begin{bmatrix} V \\ uV + p\eta_x \\ vV + p\eta_y \\ wV + p\eta_z \end{bmatrix} ; \hat{G} = \frac{1}{J}\begin{bmatrix} W \\ uW + p\zeta_x \\ vW + p\zeta_y \\ wW + p\zeta_z \end{bmatrix}$$

$$\hat{E}_\nu = \frac{(1 + \nu_t}{J}\begin{bmatrix} 0 \\ (\nabla\xi.\nabla\xi)u_\xi + (\nabla\xi.\nabla\eta)u_\eta + (\nabla\xi.\nabla\zeta)u_\zeta \\ (\nabla\xi.\nabla\xi)v_\xi + (\nabla\xi.\nabla\eta)v_\eta + (\nabla\xi.\nabla\zeta)v_\zeta \\ (\nabla\xi.\nabla\xi)w_\xi + (\nabla\xi.\nabla\eta)w_\eta + (\nabla\xi.\nabla\zeta)w_\zeta \end{bmatrix}$$

$$\hat{F}_\nu = \frac{(1 + \nu_t}{J}\begin{bmatrix} 0 \\ (\nabla\eta.\nabla\xi)u_\xi + (\nabla\eta.\nabla\eta)u_\eta + (\nabla\eta.\nabla\zeta)u_\zeta \\ (\nabla\eta.\nabla\xi)v_\xi + (\nabla\eta.\nabla\eta)v_\eta + (\nabla\eta.\nabla\zeta)v_\zeta \\ (\nabla\eta.\nabla\xi)w_\xi + (\nabla\eta.\nabla\eta)w_\eta + (\nabla\eta.\nabla\zeta)w_\zeta \end{bmatrix}$$

$$\hat{G}_\nu = \frac{(1 + \nu_t}{J}\begin{bmatrix} 0 \\ (\nabla\zeta.\nabla\xi)u_\xi + (\nabla\zeta.\nabla\eta)u_\eta + (\nabla\zeta.\nabla\zeta)u_\zeta \\ (\nabla\zeta.\nabla\xi)v_\xi + (\nabla\zeta.\nabla\eta)v_\eta + (\nabla\zeta.\nabla\zeta)v_\zeta \\ (\nabla\zeta.\nabla\xi)w_\xi + (\nabla\zeta.\nabla\eta)w_\eta + (\nabla\zeta.\nabla\zeta)w_\zeta \end{bmatrix}$$

with U, V and W are contravariant velocities:

$$U = u\xi_x + v\xi_y + w\xi_z \ ; \ V = u\eta_x + v\eta_y + w\eta_z \ ; \ W = u\zeta_x + v\zeta_y + w\zeta_z$$

and $J = det \begin{bmatrix} \xi_x & \xi_y & \xi_z \\ \eta_x & \eta_y & \eta_z \\ \zeta_x & \zeta_y & \zeta_z \end{bmatrix}$ is the Jacobian of transformation

4. Artificial compressibility method

Artificial compressibility method flow is introduced by adding a time derivative of pressure to the continuity equation. In the steady-state formulation, the equations are marched in a time-like fashion until the divergence of velocity vanishes. The time variable for this process no longer represents physical time. Therefore, in the momentum equations t is replaced with τ, which can be thought of as an artificial time or iteration parameter. As a result, the governing equations can be written in the following form:

$$\frac{\partial \hat{Q}}{\partial \tau} + \frac{\partial(\hat{E} - \hat{E}_\nu)}{\partial \xi} + \frac{\partial(\hat{F} - \hat{F}_\nu)}{\partial \eta} + \frac{\partial(\hat{G} - \hat{G}_\nu)}{\partial \zeta} = 0 \tag{9}$$

where $\hat{Q} = \frac{1}{J} \begin{bmatrix} p \\ u \\ v \\ w \end{bmatrix}$ and τ is the artificial time variable

The extension of artificial compressibility method to unsteady flow is introduced by adding physical time derivative of velocity components to three momentum equations in Equations (9) (see [4], [5] and [8]). The obtained equations can be written as:

$$\Gamma \frac{\partial \hat{Q}}{\partial \tau} + \Gamma_e \frac{\partial \hat{Q}}{\partial t} + \frac{\partial(\hat{E} - \hat{E}_\nu)}{\partial \xi} + \frac{\partial(\hat{F} - \hat{F}_\nu)}{\partial \eta} + \frac{\partial(\hat{G} - \hat{G}_\nu)}{\partial \zeta} = 0 \tag{10}$$

where $\Gamma = \begin{bmatrix} 1 & 0 & 0 & 0 \\ 0 & 1 & 0 & 0 \\ 0 & 0 & 1 & 0 \\ 0 & 0 & 0 & 1 \end{bmatrix}$ and $\Gamma_e = \begin{bmatrix} 0 & 0 & 0 & 0 \\ 0 & 1 & 0 & 0 \\ 0 & 0 & 1 & 0 \\ 0 & 0 & 0 & 1 \end{bmatrix}$

Unsteady solution at each physical time t is steady solution obtained by marching in artificial time τ.

5. Numerical Method

Discretizing Equation (9) with first order finite difference for artificial time and a backward difference for physical time term result in

$$\Gamma \frac{\hat{Q}^{k+1} - \hat{Q}^k}{\Delta \tau} + \Gamma_e \frac{(1+\phi)(\hat{Q}^{k+1} - \hat{Q}^n) - \phi(\hat{Q}^n - \hat{Q}^{n-1})}{\Delta t}$$

$$+\delta_\xi(\hat{E} - \hat{E}_\nu)^{k+1} + \delta_\eta(\hat{F} - \hat{F}_\nu)^{k+1} + \delta_\zeta(\hat{G} - \hat{G}_\nu)^{k+1} = 0 \tag{11}$$

Here k is the pseudo-iteration counter, n is the time step counter and δ represents spatial differences in the direction indicated by the subscript. When $\phi = 0$ the method is first-order temporally accurate; when $\phi = 0.5$ the method is second-order accurate. After linearlization [9], Equations (11) have the following form:

$$\begin{aligned}
&\Gamma\frac{\hat{Q}^{k+1}-\hat{Q}^{k}}{\Delta\tau}+\Gamma_e\frac{(1+\phi)(\hat{Q}^{k}+\Delta\hat{Q}^{k})-(1+2\phi)\hat{Q}^{n}+\phi\hat{Q}^{n-1}}{\Delta t}\\
&+\delta_\xi(\hat{E}^{k}+A^{k}\Delta\hat{Q}^{k})+\delta_\eta(\hat{F}^{k}+B^{k}\Delta\hat{Q}^{k})+\delta_\zeta(\hat{G}^{k}+C^{k}\Delta\hat{Q}^{k})\\
&-\delta_\xi(\hat{E}^{k}_{\nu}+A^{k}_{\nu}\Delta\hat{Q}^{k})-\delta_\eta(\hat{F}^{k}_{\nu}+B^{k}_{\nu}\Delta\hat{Q}^{k})-\delta_\zeta(\hat{G}^{k}_{\nu}+C^{k}_{\nu}\Delta\hat{Q}^{k})
\end{aligned} \tag{12}$$

where $\Delta\hat{Q}^{k}=\hat{Q}^{k+1}-\hat{Q}^{k}$, A, B, C, A_ν, B_ν and C_ν are the convective flux and viscous flux with respect to $\hat{Q}$.

$$A=\frac{\partial\hat{E}}{\partial\hat{Q}}\ ;\ B=\frac{\partial\hat{F}}{\partial\hat{Q}}\ ;\ C=\frac{\partial\hat{G}}{\partial\hat{Q}}\ ;\ A_\nu=\frac{\partial\hat{E}_\nu}{\partial\hat{Q}}\ ;\ B_\nu=\frac{\partial\hat{F}_\nu}{\partial\hat{Q}}\ ;\ C_\nu=\frac{\partial\hat{G}_\nu}{\partial\hat{Q}}$$

Rewriting Equations (12) such that all terms evaluated at sub-iteration k or time step n and $n-1$ are on the right hand side and all term multiplying $\Delta\hat{Q}^{k}$ are on the left hand side

$$\left(\Gamma+\Gamma_e\frac{(1+\phi)\Delta\tau}{\Delta t}+\Delta\tau(\delta_\xi A^{k}+\delta_\eta B^{k}+\delta_\zeta C^{k}-\delta_\xi A^{k}_{\nu}-\delta_\eta B^{k}_{\nu}-\delta_\zeta C^{k}_{\nu})\right)\Delta\hat{Q}^{k}=R^{k} \tag{13}$$

where

$$\begin{aligned}
R^{k}=&-\Delta\tau\left(\Gamma_e\frac{(1+\phi)\hat{Q}^{k}-(1+2\phi)\hat{Q}^{n}+\phi\hat{Q}^{n-1}}{\Delta t}\right)\\
&-\Delta\tau(\delta_\xi\hat{E}^{k}+\delta_\eta\hat{F}^{k}+\delta_\zeta\hat{G}^{k}-\delta_\xi\hat{E}^{k}_{\nu}-\delta_\eta\hat{F}^{k}_{\nu}-\delta_\zeta\hat{G}^{k}_{\nu})
\end{aligned}$$

Equations (13) is solved by applying an approximate factorization technique with the use of ADI type scheme. The detailed description of this procedure can be found in [10]. The viscous terms are approximated by central difference expressions, while the flux splitting procedure is applied to convective terms [11]. For example, Jacobian matrix A in Equations (13) may be expressed as:

$$A=K\Lambda K^{-1} \tag{14}$$

where Λ is the diagonal matrix formed by the eigenvalues of A, namely

$$\Lambda=\begin{bmatrix}\lambda_1&0&0&0\\0&\lambda_2&0&0\\0&0&\lambda_3&0\\0&0&0&\lambda_4\end{bmatrix} \tag{15}$$

The matrix K is

$$K = \left[K^{(1)}, K^{(2)}, K^{(3)}, K^{(4)}\right] \tag{16}$$

where the column $K^{(i)}$ is the right eigenvectors of A corresponding to λ_i and K^{-1} is the inverse of K.

The splitting are performed as

$$A = A^+ + A^- \quad with \quad A^{\pm} = K\Lambda^{\pm}K^{-1} \tag{17}$$

where

$$\Lambda^- = \begin{bmatrix} \lambda_1^- & 0 & 0 & 0 \\ 0 & \lambda_2^- & 0 & 0 \\ 0 & 0 & \lambda_3^- & 0 \\ 0 & 0 & 0 & \lambda_4^- \end{bmatrix} \quad ; \quad \Lambda^+ = \begin{bmatrix} \lambda_1^+ & 0 & 0 & 0 \\ 0 & \lambda_2^+ & 0 & 0 \\ 0 & 0 & \lambda_3^+ & 0 \\ 0 & 0 & 0 & \lambda_4^+ \end{bmatrix} \tag{18}$$

with definitions

$$\lambda_i^- = \frac{1}{2}\left(\lambda_i - |\lambda_i|\right) \quad ; \quad \lambda_i^+ = \frac{1}{2}\left(\lambda_i + |\lambda_i|\right) \tag{19}$$

Using the splitting of A given by (17), spatial difference operator of A can be derived as

$$\delta_\xi A = \delta_\xi^+ A + \delta_\xi^- A \tag{20}$$

where δ_ξ^- and δ_ξ^+ are backward and forward difference operators, respectively. The similar procedures are applied to spatial difference operator of B and C in Equations (13).

6. Turbulence modeling

In the calculations presented in this paper, the model $k-\varepsilon$ of Chien [12] for low Reynolds number flows is employed. Transport equations for turbulent kinetic energy k and its dissipation rate ε are as follow,

$$\frac{\partial(\rho k)}{\partial t} + \frac{\partial(\rho u_j k)}{\partial x_j} = \frac{\partial}{\partial x_j}\left((\mu + \frac{\mu_t}{\sigma_k})\frac{\partial k}{x_j}\right) + P_k - \rho\varepsilon + S_k = 0 \tag{21}$$

$$\frac{\partial(\rho \varepsilon)}{\partial t} + \frac{\partial(\rho u_j \varepsilon)}{\partial x_j} = \frac{\partial}{\partial x_j}\left((\mu + \frac{\mu_t}{\sigma_k})\frac{\partial \varepsilon}{x_j}\right) + c_1 f_1 P_k - c_2 f_2 \rho\varepsilon + S_\varepsilon = 0 \tag{22}$$

where

$$P_k = \tau_{ij}\frac{\partial u_i}{\partial x_j} \quad ; \quad \tau_{ij} = -\frac{2}{3}\rho k + 2\mu_t\left(S_{ij} - \frac{1}{3}\frac{\partial u_k}{\partial x_k}\delta_{ij}\right]$$

$$S_{ij} = \frac{1}{2}\left(\frac{\partial u_i}{\partial x_j} + \frac{\partial u_j}{\partial x_i}\right) \quad ; \quad \mu_t = c_\mu f_\mu \rho \frac{k^2}{\varepsilon}$$

The constants and functions are given as,

$$c_\mu = 0.99 \ ; \ c_1 = 1.35 \ ; \ c_2 = 1.8 \ ; \ \sigma_k = 1.0 \ ; \ \sigma_\varepsilon = 1.3 \ ; \ S_k = -2\mu\frac{k}{y_d^2}$$

$$S_\varepsilon = -2\mu\frac{\varepsilon}{y_d^2}\exp(-0.5y^+) \;\; ; \;\; f_1 = 1.0 \;\; ; \;\; f_2 = 1.0 - 0.22\exp\left[-\left(\frac{R_T}{6}\right)^2\right]$$

$$f_\mu = 1.0 - \exp(0.0115y^+) \;\; ; \;\; R_T = \frac{k^2}{\nu\varepsilon} \;\; ; \;\; y^+ = \frac{y_d u_\tau}{\nu}$$

where y_d is distance to the wall and u_τ is friction velocity.

Similar to Equations (1), Equations (21) and (22) are put into non-dimensional form and transformed into generalized curvilinear coordinate (ξ, η, ζ). The solution algorithm uses the first-order implicit difference for unsteady term, the first-order upwind difference for convective term and the second-order central difference for viscous terms. Because the equations for k and ε are much stiffer than the flow equations [13], these turbulence equations are solved separately for each time step. The obtained solution is used to calculate the turbulent viscosity for next time step.

7. Initial and boundary conditions

The governing equations (1) or (8) and turbulence model equations (21) and (22) require initial condition to start the calculation as well as boundary conditions at every time step.

In the calculations presented in this paper, the uniform free-stream values are use as initial conditions:

$$p = p_\infty \;\; ; \;\; u = u_\infty \;\; ; \;\; v = v_\infty \;\; ; \;\; w = w_\infty \;\; ; \;\; k = k_\infty \;\; ; \;\; \varepsilon = \varepsilon_\infty \tag{23}$$

For external flow applications, the far-field bound is placed far away from the solid surface. Therefore, the free-stream values are imposed at the far-field boundary except along the outflow boundary where extrapolation for velocity components in combination with $p = p_\infty$ is used to account for the removal of vorticity from the flow domain by convective process [14].

On the solid surface, the no-slip condition is imposed for velocity components:

$$u = 0 \;\; ; \;\; v = 0 \;\; ; \;\; w = 0 \tag{24}$$

The surface pressure distribution is determine by setting the normal gradient of pressure to be zero:

$$\frac{\partial p}{\partial n} = 0 \tag{25}$$

The turbulent kinetic energy and normal gradient of its dissipation rate are required to be zero on the solid boundary:

$$k = 0 \;\; ; \;\; \frac{\partial \varepsilon}{\partial n} = 0 \tag{26}$$

8. Numerical results and comparison to experiment

We tested the computation method presented here for two cases including flow past a circular cylinder and flow around a hemispherical head of a cylindrical object.

8.1. Flow pas a circular cylinder.

The experiment was carried out by Ong and Wallace [15] for flow past a circular cylinder with the Reynolds number $Re = \frac{U_0 D}{\nu} = 3900$. Here U_0 is free-stream velocity and D is the diameter of cylinder. Our numerical simulation used a boundary-fitted curvilinear coordinates grid system of 163 nodes in the circular direction (ξ) and 132 nodes in the radial direction (η). The calculation domain and a close view of calculation grid are shown in Fig. 1. In order to increase the resolution in regions where gradients are large, the grid lines in the radial direction (η) were clustered near the surface. The distance between two consecutive nodes in the radial direction started from 4.52×10^{-5} near the solid surface, increased by a factor of 1.0848.

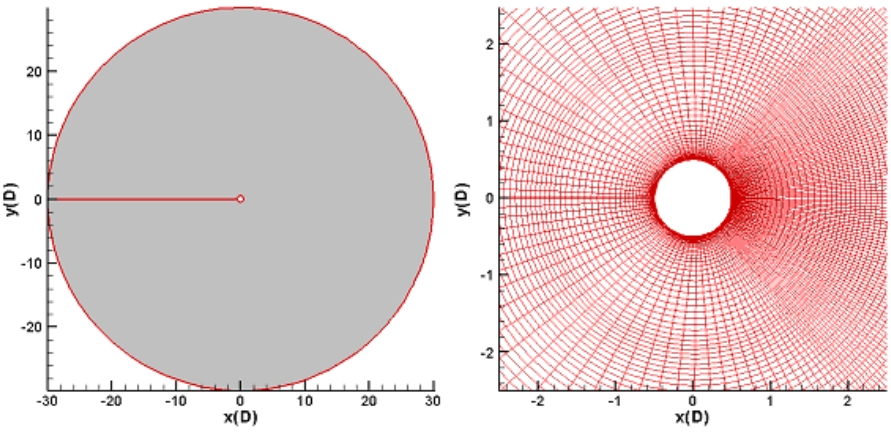

FIG. 1. Calculation domain (left) and a close view of the calculation grid (right)

The computation was performed with a non-dimensional time step $\Delta t = 1.5 \times 10^{-2}$. A statically converged mean flow field was obtained after 2000 time steps. Fig. 2 shows distribution of pressure and longitudinal velocity component U near the object at $t = 2000\Delta t$. The non-dimensional values are given in these figures by using Equation (4) with the reference length is the diameter D of cylinder and the reference velocity is the free-stream velocity U_0. A region of low pressure is formed behind the object. In front of object, pressure strongly varies and a region of high pressure is formed near separation point and two regions of low pressure are developed next. From Fig. 2, it can be seen the

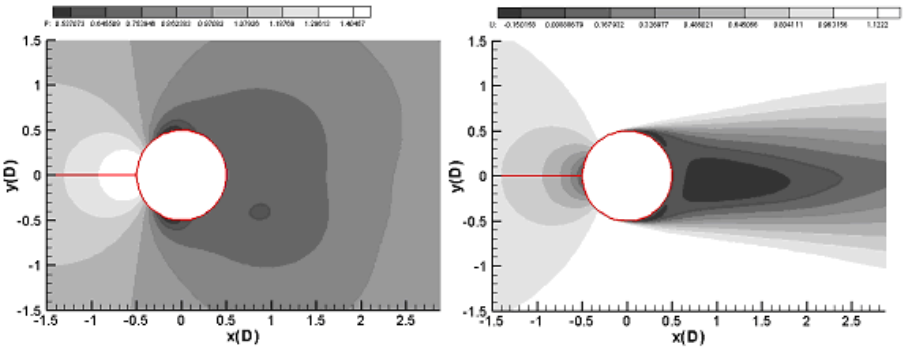

FIG. 2. Contour plots of pressure (left) and longitudinal velocity component U (right) near the cylinder

development of a recirculation zone behind the object with reverse velocity.

The calculated results are compared with the corresponding experimental data. Fig. 3(a) compares the mean measured and calculated pressure coefficients $C_p = \frac{p-p_\infty}{0.5\rho V_\infty^2}$ along the object. The agreement of calculated results with experimental data is quite good, especially in the front region. Fig. 3(b) compares the profile of mean longitudinal velocity component at a location in the wake behind the cylinder. For this calculated mean cross-flow velocity profile, the agreement with experimental result is also good.

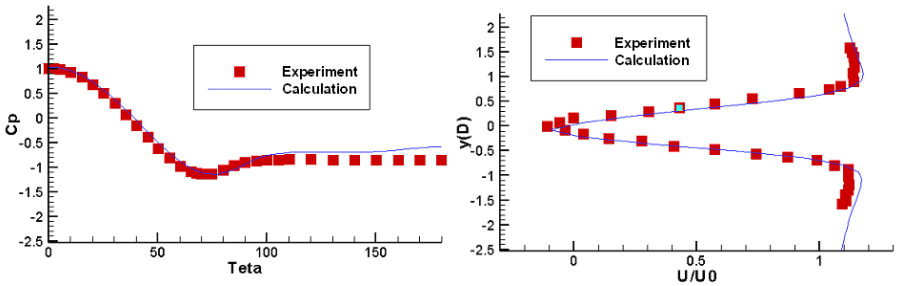

FIG. 3. Comparison between numerical simulation with measurement: (a) mean pressure coefficient along object surface (b) profile of mean longitudinal velocity component at $x = 1.54D$

8.2. Flow around a hemispherical head of a cylindrical object.

The second test case was performed for a flow around a hemispherical head of a cylindrical object at zero-degree angle of attack (see Fig. 4). The experiment was carried out by Rouse and McNown [16]. The Reynolds number is 1.36×10^5 based on the inflow velocity and the diameter of hemisphere.

The 3D grid system has 82x132x37 nodes in the streamwise direction (ξ), radial

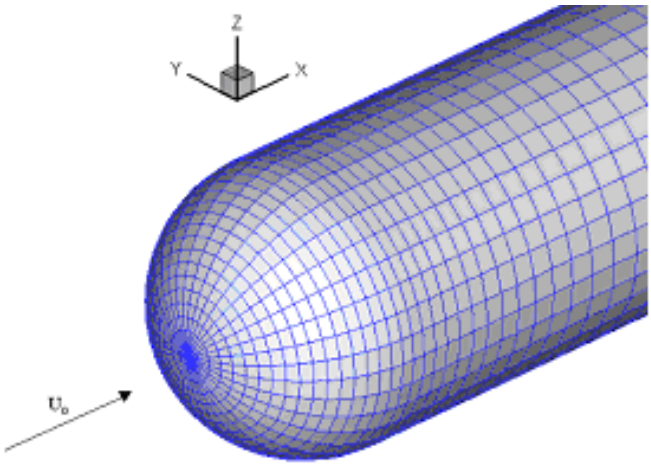

FIG. 4. Diagram of the experiment and grid lines at plane $\eta = 0$ (object surface)

direction (η) and azimuthal direction (ζ), respectively. The grid lines were clustered both near the surface as well as at the bend where the hemisphere meets with the cylinder. A close view of calculating grid at plane $\eta = 0$ is also shown in Fig. 4. The calculation domain and a close view of calculation grid at a plane $\zeta = const$ are shown in Fig. 5.

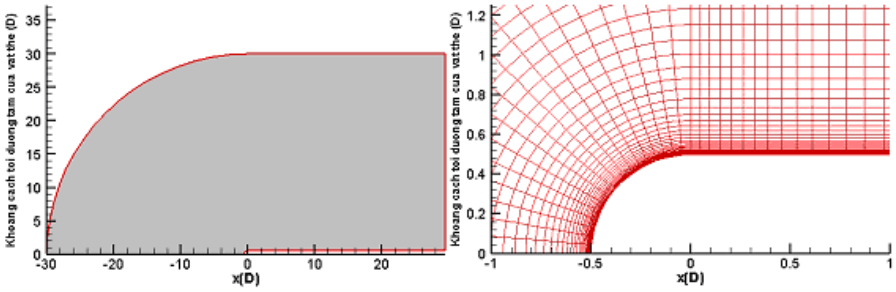

FIG. 5. Calculation domain and a close view of calculation grid at a plane $\zeta = const$

The computation was performed with a non-dimensional time step $\Delta t = 5 \times 10^{-3}$. A converged mean flow field was obtained after 5000 time steps. Analysis of the calculated results shows that flow is steady and axisymmetric. This result is suitable to experimental observations. Fig. 6a shows the distribution of pressure near the objects. The non-dimensional values are given in this figure. It can be seen from Fig. 6a that a region of low pressure is formed at the bend where the hemisphere meets with the cylinder. The region of high pressure can be seen at the separation point of flow. Fig 6b compares

measured and calculated surface pressure distributions. It can be seen that the calculated results match the experiment data quite well.

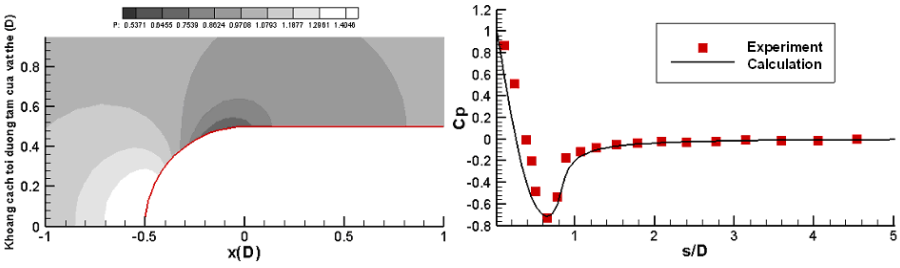

FIG. 6. Some calculated results of pressure: (a) Pressure distribution at a plane $\zeta = const$; (b) Comparison with experimental data

9. Conclusion

A method for the solution of incompressible Navier-Stokes equations in three-dimensional generalized curvilinear coordinates is presented. The method can be used to compute both steady-state and time-dependent flow problems. The method is based on artificial compressibility algorithm and uses a one-order flux splitting technique for convective terms and a second-order central difference for viscous terms. The flows around a circular cylinder and around a hemispherical head of a cylindrical object are calculated and the results are compared with experimental data. Good agreements is observed. The method can be directly applied to many practical problems.

Acknowledgments. This work is supported in part by Natural Science Council of Vietnam

References

1. S. V. Patankar, *Numerical Heat Transfer and Fluid Flow*, McGraw-Hill Book Company, New York, 1980
2. J. P. Van Doormaal, G.D Raithby, Enhancement of the SIMPLE method for predicting incompressible fluid flows, *Numer. Heat Transfer*, Vol **7**(1984), 147–163.
3. A. J. Chorin, A Numerical Method for Solving Incompressible Viscous Flow Problem, *J. Comput. Phys.,* Vol **2**(1967), 12–26.
4. C. L. Mercle, M. Athavale, *Time-Accurate Unsteady Incompressible Flow Algorithms Based on Artificial Compressibility,* AIAA Paper 87-1137, AIAA Press Washington, DC, 1987.

5. W. G. Park, L. N. Sankar, *A Technique for the Prediction of Unsteady Incompressible Viscous Flows*, AIAA Paper 93-3006, AIAA Press, Washington, DC, 1993.
6. P. L. Roe, Approximate Riemann Solvers, Parameter Vectors, and Difference Schemes, *J. Comput. Phys.,* Vol **43**(1981), 357–372.
7. P. Knupp, **Fundamentals of Grid Generation,** CRC Press Florida, 1984.
8. D. Kwak, S. Rogers, S. Yoon, J. Chang, *Numerical Solution of Incompressible Navier-Stokes Equations,* In "Computational Fluid Dynamics Techniques", Ed. by W. Habashi and M. Hafez, Gordon and Breach Pub., Amsterdam, 1995, 367–396.
9. T. J. Barth, *Analysis of Implicit Local Linearization Techniques for Upwind and TVD Algorithms*, AIAA Paper 87-0595, AIAA Press, Washington, DC, 1987.
10. S. Pandya, S. Venkateswaran, T. Pulliam, *Implementation of Preconditioned Dual-Time Procedures in OVERFLOW,* AIAA Paper 2003-0072, AIAA Press, Washington, DC, 2003.
11. E. F. Toro, *Riemann Solvers and Numerical Methods for Fluid Dynamics - A Practical Introduction, Second Edition,* Springer-Verlag, Berlin, 1999.
12. K. Y. Chien, Prediction of Change and Boundary Layer Flows with a Low-Reynolds-Number Turbulence Model, *AIAA Journal*, Vol **22**(1982), 33–38.
13. J. H. Ferziger, M. Perie, *Computational Method for Fluid Dynamics,* Springer-Verlag, Berlin, 1996.
14. W. G. Park, A Three-dimensional Multigrid Technique for Unsteady Imcompressible Viscous Flow, *Ph. D. Thesis, Georgia Institute of Technology,* Atlanta, Georgia, 1988.
15. L. Ong, J. Wallace, The Velocity Field of the Turbulence Very Near Wake of a Circular Cylinder, *Exp. Fluids*, Vol **20**(1996), 441–453.
16. H. Rouse, J. S. McNown, *Cavitation and Pressure Distribution, Head Forms at Zero Angle of Yaw,* Studies in Engineering, Bulletin 32, State University of Iowa, 1948.